Automatic Extraction of Permanent Ground Offset from Near-Field Accelerograms: Algorithm, Validation, and Application to the 2004 Parkfield Earthquake

Asaf Inbal*[1] and Alon Ziv[1]

ABSTRACT

Permanent ground offsets, constituting a prime dataset for constraining final fault-slip distributions, may not be recovered straightforwardly by double integration of near-field accelerograms due to tilt and other distorting effects. Clearly, if a way could be found to recover permanent ground offsets from acceleration records, then static datasets would be enlarged, and thus the resolution of fault-slip inversions would be enhanced. Here, we introduce a new approach for extracting permanent offsets from near-field strong-motion accelerograms. The main advantage of the new approach with respect to previous ones is that it corrects for source time functions of any level of complexity. Its main novelty is the addition of a constraint on the slope of the ground velocity spectra at long periods. We validated the new scheme using collocated accelerograms and Global Navigation Satellite Systems (GNSS) records of the 2011 M_w 9 Tohoku-Oki earthquake. We find a good agreement between accelerogram-based and GNSS-based ground offsets over a range of 0.1–5 m. To improve the spatial coverage of permanent ground offsets associated with the 2004 Parkfield earthquake, near-field accelerograms were baseline corrected using the new scheme. Static slip inversion of the combined GNSS-based and accelerogram-based ground displacements indicates appreciable seismic moment release south of the epicenter, about 5 km into the Cholame section of the San Andreas fault. We conclude that the strong shaking observed to the south of the epicenter is directly related to the slip in that area and is not the result of local amplification.

KEY POINTS

- WA new technique for extracting permanent ground offset from near-field accelerograms is introduced.
- The new scheme is validated using collocated strong motion and Global Positioning System (GPS) records of the 2011 Tohoku-Oki earthquake.
- A new 2004 Parkfield slip model is presented that uses the combined strong motion and GPS dataset.

INTRODUCTION

In addition to a transient component, the ground motion near strong earthquakes includes a geodetically observable component of permanent offset, the contribution of which rises with decreasing distance from the earthquake focus (Fig. 1). These transient and permanent ground motions are commonly referred to as the far-field and the near-field components of the radiated elastic wavefield, respectively (Aki and Richards, 2002). Because permanent ground offsets are far less sensitive to the subsurface structure than transient motions are, and are more directly related to the final deformation at depth, they constitute a prime dataset for constraining the final fault-slip distributions (Segall, 2010). To date, however, near-field permanent offsets cannot be recovered straightforwardly through double integration of near-field accelerograms as these are often distorted by baseline shifts (e.g., Iwan *et al.*, 1985; Boore, 2001; Wu and Wu, 2007; Melgar *et al.*, 2013). A common cause for acceleration baseline shift is ground tilt, the effect of which is to shift the horizontal and vertical baselines according to

---

1. Department of Geophysics, Tel Aviv University, Tel Aviv, Israel

*Corresponding author: asafinbal@tauex.tau.ac.il

Cite this article as Inbal, A., and A. Ziv (2020). Automatic Extraction of Permanent Ground Offset from Near-Field Accelerograms: Algorithm, Validation, and Application to the 2004 Parkfield Earthquake, *Bull. Seismol. Soc. Am.* **XX**, 1–9, doi: 10.1785/0120200040

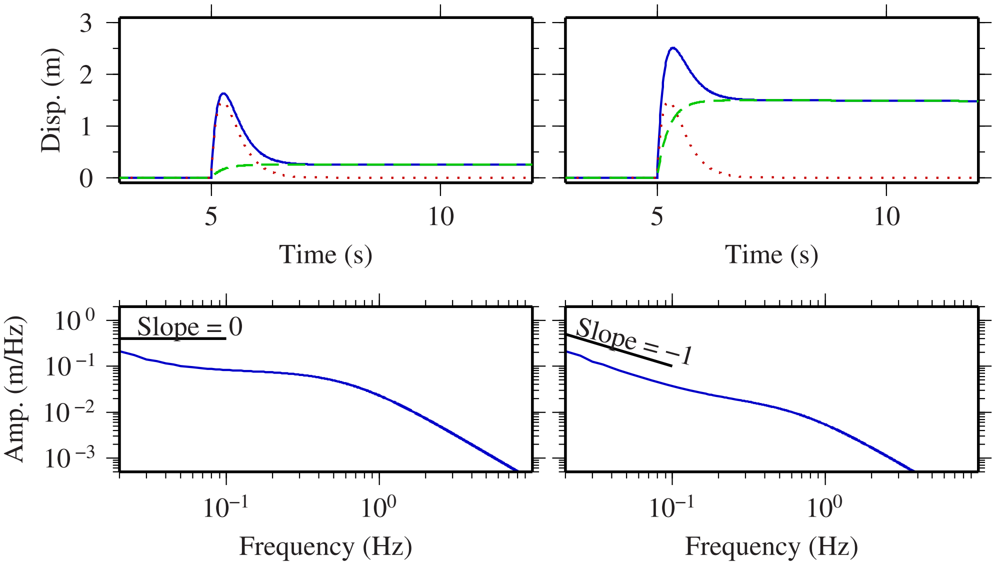

Figure 1. Example ground motions combining Brune-type near-field and far-field components. Ground displacement and displacement spectra are shown in top and bottom panels, respectively. The situation of far-field component greater than near-field component is shown in the left panels, and that of near-field component greater than far-field component is shown in the right panels. Near-field, far-field, and the sum of the two are indicated by solid, dashed, and dotted curves, respectively. The color version of this figure is available only in the electronic edition.

$$\Delta g_{\mathrm{hor}} = g \sin(\theta) \quad \text{and} \quad \Delta g_{\mathrm{ver}} = g(1 - \cos(\theta)), \tag{1}$$

with g being the reference gravitational acceleration, θ being the tilt angle, and the superscripts hor and ver standing for the horizontal and vertical components, respectively. For very small tilts, when $\theta \to 0$, the horizontal baseline shift is proportional to θ, and the vertical shift is proportional to $0.5\theta^2$. Consequently, even a very small tilt, say 10^{-5} radians, can cause about 20 cm of drift in the horizontal static offset within only 1 min from the tilt event. Such drifts are easily recognized by visual inspection; instead of flattening after transient motion has ceased, near-field double-integrated accelerograms vary (increase or decrease) as a quadratic function of time. To obtain accurate static offsets, the acceleration time series must be corrected before it is integrated. It is worth noting that additional causes for acceleration baseline offset include the transducer's response to strong shaking and/or problems in the AD converter (Boore, 2001).

Clearly, if a way could be found to recover permanent ground offsets from accelerograms, then static datasets would be enlarged and their spatial coverage improved, and thus the resolution of fault-slip inversions would be enhanced. This would be most advantageous in cases in which Interferometric Synthetic Aperture Radar (InSAR) and optical imagery contain a considerable amount of postseismic deformation and/or the fault orientation is unfavorable for InSAR observations. It would also be advantageous in seismically active regions withcontinuous geodetic coverage that is sparse.

In addition to finite fault-slip applications, rapid permanent offset extraction may also be used for earthquake rapid response and on-land local tsunami alert systems. These lines of thinking have motivated several researchers to seek ways to extract permanent ground offset from near-fault accelerograms experiencing baseline shifts.

This article is organized as follows: first, available approaches for correcting near-field accelerograms are described along with their shortcomings. Second, a new scheme for extracting the permanent ground offsets from strong-motion (SM) accelerograms is introduced. The new scheme is then validated using collocated SM and Global Navigation Satellite Systems (GNSS) records of the 2011 M_w 9 Tohoku-Oki earthquake. Third, the new approach is used for augmenting and improving the spatial coverage of the permanent ground offsets associated with the 2004 Parkfield earthquake. Finally, a new 2004 Parkfield slip model is presented that uses this combined dataset.

PREVIOUS STUDIES

If continuous displacement data are available from collocated high-rate GNSS receivers, then these data may be used to correct the SM accelerograms (e.g., Nikolaidis *et al.*, 2001; Emore *et al.*, 2007; Bock *et al.*, 2011; Melgar *et al.*, 2013). Yet, only a few modern seismic networks operate both SM and high-rate GNSS instruments, and even in these so called seismogeodetic networks, only a small subset of the GNSS monuments are collocated with accelerometers. It is therefore useful to provide a correction scheme that does not rely on accurate long-period measurements from a nearby GNSS receiver. In the following, commonly used approaches for correcting distorted SM data are described.

Iwan *et al.* (1985) introduced a scheme for obtaining permanent offsets through double integration of SM accelerograms. According to this approach, corrections are applied to two consecutive intervals of the acceleration time series. The earliest data interval between t_1 and t_2 begins at the onset of strong ground motion and ends when SM has resided, and the subsequent interval starts at t_2 and ends at the end of the record. The correction applied to times greater than t_2, with a

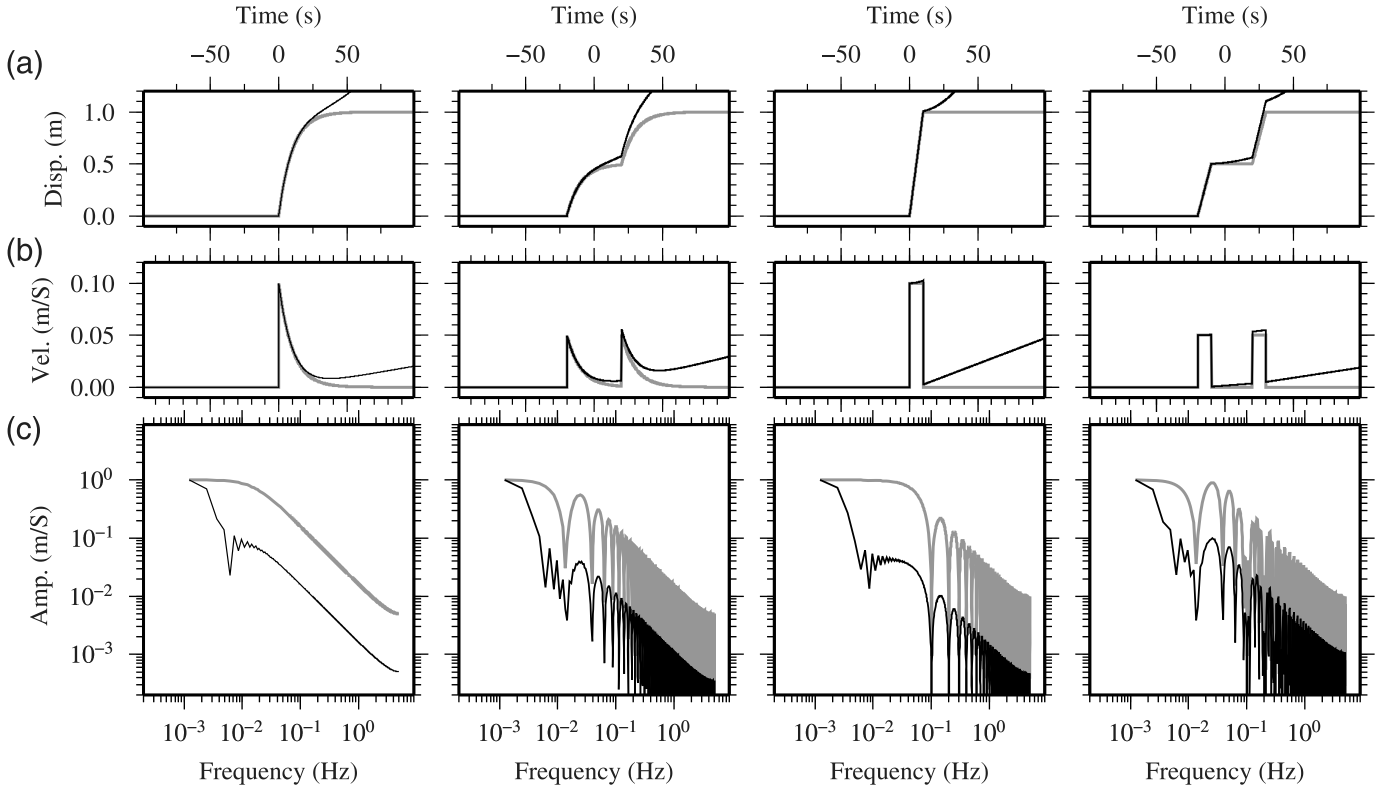

Figure 2. Various synthetic source time functions with and without baseline offset and their corresponding velocity spectra. (a) Displacement, (b) velocity, and (c) velocity spectra are shown. Black and gray curves indicate records with and without baseline offset, respectively.

factor of a_f, is obtained by least-square fitting the integrated accelerograms to the following linear function:

$$v_f(t) = v_0 + a_f t, \quad (2)$$

in which v_0 and a_f are the fitting coefficients. The correction applied to the earliest interval between t_1 and t_2 is

$$a_m = v_f(t_2)/(t_2 - t_1). \quad (3)$$

As already noted by Boore (2001), the permanent offsets resulting from the application of the bilinear correction of Iwan *et al.* (1985) are sensitive to the choice of t_1 and t_2, which may not be determined by visual inspection of the acceleration records or use of simple rule of thumb as suggested by Iwan *et al.* (1985). It is worth noting that Graizer (1979) introduced an optimization approach for minimizing the baseline shift following strong shaking in which the integrated acceleration is approximated using a set of polynomial functions. The best-fitting polynomials are differentiated and removed from the acceleration to obtain the correction terms. The choice of the polynomial functions is, however, subjective (Boore *et al.*, 2002).

The subsequent studies of Wu and Wu (2007) and Wang *et al.* (2011) adopted the bilinear correction of Iwan *et al.* (1985) and introduced criteria for setting t_1 and t_2 objectively. The former determined t_1 and t_2 iteratively by minimizing the residual between the twice-integrated SM accelerogram and a ramp shape, whereas the latter did so by replacing the ramp function with a step function. The main shortcomings of these model-based approaches are that they do not account for multiple slip episodes and they make stringent assumptions regarding the shape of the source time function. Despite these limitations, the approaches of Wu and Wu (2007) and Wang *et al.* (2011) yield reasonable agreement with independent measurements of static offset using borehole accelerograms, even for earthquakes with complex rupture histories and several well-resolved slip episodes recorded by borehole accelerometers (Wang *et al.*, 2013). In contrast, the static offsets extracted via this approach from surface accelerometers experiencing strong shaking are less reliable (Melgar *et al.*, 2013). The new scheme described in the following completely relaxes the assumptions underlying its predecessors, thus providing more robust accurate static offsets.

ALGORITHM DESCRIPTION

Key principles underlying the new approach described here are illustrated in Figure 2, which compares different synthetic source time functions with and without a baseline offset and their corresponding velocity spectra. Two useful insights emerge from this exercise: (1) for frequencies well below the corner frequency, the velocity spectra is flat and is insensitive to the shape of the static time series and (2) the amplitude of the low-frequency asymptote is equal to the static offset. Both conclusions are in

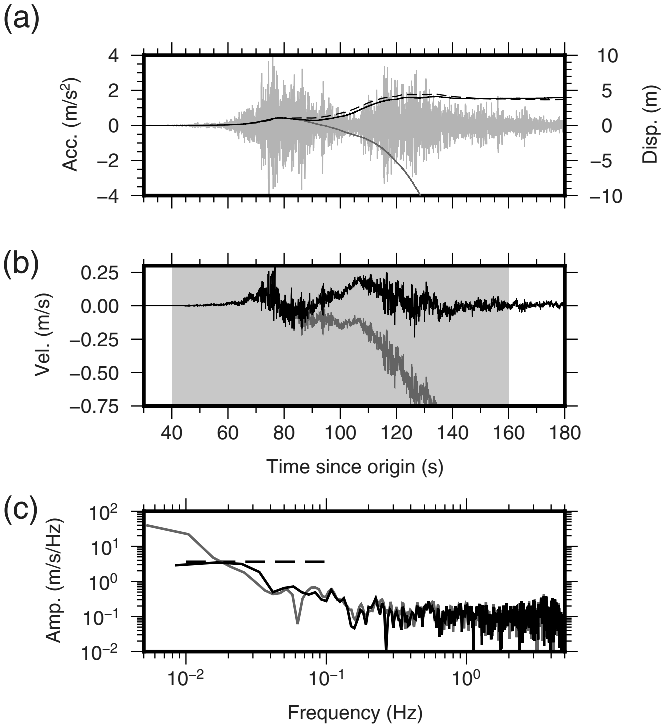

Figure 3. Analysis of east–west motion at near-field station MYG001 collocated with Global Navigation Satellite Systems (GNSS) site p0172 (see also Fig. 4). (a) Acceleration and displacement as a function of time, (b) velocity as a function of time, and (c) velocity spectra computed for the interval indicated by the gray rectangle in panel (b), with black dashed curve indicating static offset measured at the GNSS site. Thick black and dark gray displacement curves are for baseline-corrected and raw strong-motion (SM) data, respectively, and black dashed curve is for GNSS data.

line with previous well-established theoretical results (e.g., Brune, 1970; Madariaga, 1976; Vidale *et al.*, 1995) and observations (Madariaga *et al.*, 2018) and are taken into account in the design of the new algorithm. The most notable modification with respect to previous algorithms is related to the criteria for selecting t_1 and t_2. Although the new scheme implements an iterative procedure for selecting t_1 and t_2 as in Wu and Wu (2007) and Wang *et al.* (2011), the criterion used here for selecting the $t_1 - t_2$ interval is checked in the frequency domain rather than in the time domain. Thanks to this modification, the new scheme can handle any shape of source time function, is not restricted to a specific number of slip pulses, and may be executed automatically.

The new automatic scheme for extracting permanent offsets from SM accelerograms progresses along the following steps:

1. Identify t_f, the time at which the cumulative ground-motion energy reached 90% of the total energy.
2. Perform a grid search over t_1 and t_2 at increments of 0.1 s, subject to $t_2 \le t_f$ and t_1, and for each $t_1 - t_2$ interval:
   - 2a. Determine a_f and v_0 by least-square fitting (equation 2) to the integrated accelerogram for $t > t_2$, and compute the first cost function (CF) as

$$\mathrm{CF}_1 = 1 - |R|, \tag{4}$$

     with R being the correlation coefficient between observed and modeled velocity.
   - 2b. Given a_f and v_0 from the previous step, determine a_m using equation (3).
   - 2c. Correct the accelerograms by subtracting a_m between t_1 and t_2 and subtracting a_f from t_2 onward.
   - 2d. Fourier transform the integrated postcorrection accelerograms, and perform linear least-square fit to the velocity spectra below the corner frequency (i.e., linear on a log–log space). Compute the second and third CFs as

$$\mathrm{CF}_2 = |b|, \tag{5a}$$

$$\mathrm{CF}_3 = \frac{\sum_j \left|\tilde{\ddot{u}}_j^{\mathrm{mod}} - \tilde{\ddot{u}}_j^{\mathrm{obs}}\right|}{\sum_j \tilde{\ddot{u}}_j^{\mathrm{mod}}}, \tag{5b}$$

     with b being the slope of the best-fitting curve subject to $-1 < b < 1$ and the third CF being the normalized L1-norm of the difference between modeled and observed velocity spectra.
   - 2e. Calculate a permanent offset by twice integrating the corrected accelerograms and a corresponding global CF as $\mathrm{CF} = \max(\mathrm{CF}_1, \mathrm{CF}_2, \mathrm{CF}_3)$.
3. Output the permanent offset corresponding to the smallest CF.The previous scheme is implemented on each channel separately. Next, it is validated using collocated SM and GNSS records of the 2011 M_{w} 9.0 Tohoku-Oki earthquake.

VALIDATION USING COLLOCATED SM AND GNSS RECORDS OF THE TOHOKU-OKI EARTHQUAKE

The Tohoku-Oki earthquake is chosen for validating our approach because (1) it caused large permanent offsets throughout Japan, (2) it was recorded by a large number of SM sensors that are collocated with 1 sample per second GNSS receivers, and (3) its source time function consisted of multiple episodes (at least two). The latter feature, well captured by the SM records (Fig. 3), may bias the static offset estimates of Wang *et al.* (2013), obtained using the time-domain approach of Wang *et al.* (2011).

Data used in this study were recorded by surface accelerometers of KiK-net and K-net networks. Surface accelerometers are more suitable for this study than borehole accelerometers because they are located closer to and at the same height as the GNSS receivers. In addition, the surface installations are more abundant worldwide and are more susceptible to baseline shifts than the borehole installations. The analysis is limited to channels with static to dynamic offset ratios (recorded by the GNSS) larger than 20%. The spatial distribution of selected GNSS and SM sites across Honshu provides diverse local site conditions

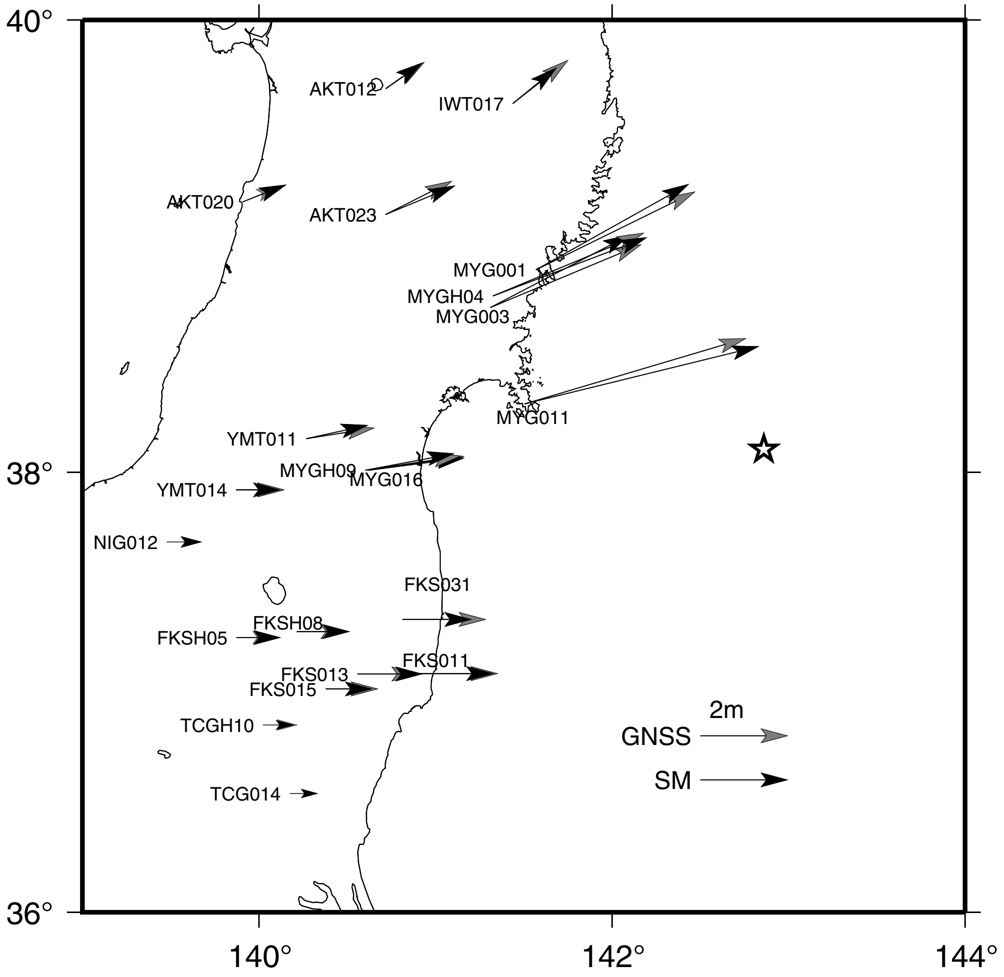

Figure 4. Map showing the K-net and KiK-net SM sites. The horizontal displacements from baseline-corrected double-integrated SM and the GNSS data are indicated by the black and grey arrows, respectively. The star indicates the Tohoku-Oki epicenter.

(Fig. 4). Yet, a correlation between local site conditions (i.e., hard rock versus soft sediment) and the discrepancy between GNSS and SM-derived offsets was not found.

Example time lines and spectra of precorrection and postcorrection ground motions at K-net site MYG001 are shown in Figure 3 for the east–west component. These are compared with the displacement recorded at GNSS site p0172. The GNSS receiver and SM station are separated by about 500 m, a distance at which differences in true permanent offsets between the sites are small. That the double-integrated precorrection acceleration curve (dashed line) falls at an accelerated rate, well after the GNSS time series (thick gray curve) has reached a plateau, is consistent with an acceleration baseline being shifted. Similar to the synthetic examples presented in Figure 2, the effect of acceleration baseline shift is to steepen the low-frequency part of the velocity spectra, which precludes the recovery of permanent offset from the raw velocity spectra. After applying the baseline correction scheme, the long-period velocity spectra becomes flat (Fig. 3c), as expected from ground-velocity records dominated by the near-field term, and the double-integrated accelerogram matches well the displacement time series recorded at site p0172 (Fig. 3a). The offset inferred from the baseline-corrected accelerogram is in good agreement with that measured at the GNSS site.

Finally, accelerogram-based and GNSS-based permanent offsets are compared in Figure 5. Good agreement between the two estimates is found, with an average discrepancy of 10%. Somewhat larger discrepancies are found for sites experiencing offsets smaller than 2 meters, presumably due to the unmodeled effect of the transient deformation field. Next, the new scheme is used for augmenting and improving the spatial coverage of the permanent ground offsets associated with the 2004 Parkfield earthquake.

IMPLICATIONS FOR THE COSEISMIC SLIP OF THE 2004 PARKFIELD EARTHQUAKE

The 2004 Parkfield earthquake ruptured a ~30 km long segment of the San Andreas fault (SAF). In addition to its unique position between creeping and presently locked sections of the SAF, the Parkfield segment was probably also the site of the 1857 M_w 7.9 Fort Tejon hypocenter, as well as its two widely felt foreshocks (Sieh, 1978). Yet, the most intriguing observation related to the Parkfield segment is the quasiperiodic recurrence of $M_w \approx 6$ earthquakes along its length. This has raised hopes that future earthquakes in this area may be predicted and prompted the deployment of a dense seismogeodetic near-fault observatory in that area (Bakun and Lindh, 1985). Despite this unprecedented monitoring effort, the inference of Parkfield's coseismic slip distribution has been hindered by two main factors. The first is that its InSAR data contain an appreciable amount of postseismic slip, and the second is that the spatial distribution of the GNSS stations were highly asymmetric with respect to the 2004 epicenter. Although all 12 GNSS stations that were available at the time of the 2004 Parkfield earthquake were located to the northwest of its epicenter, the 59 accelerometers were more evenly distributed about the epicenter and more

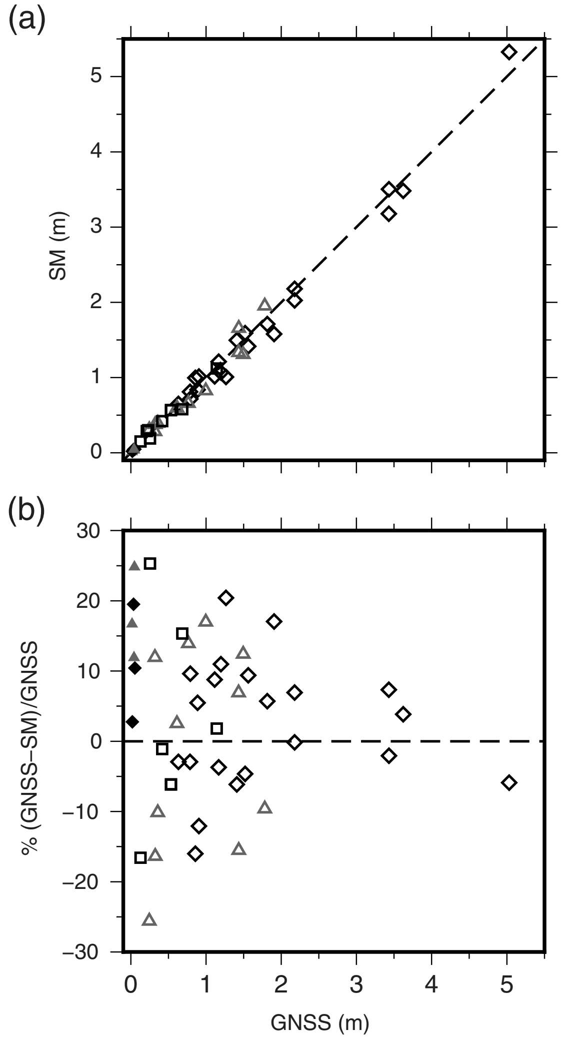

Figure 5. Comparison between permanent offsets derived from baseline-corrected SM accelerograms and the static offset measured at the nearest GNSS site. (a) SM-based as a function of GNSS-based permanent offsets. (b) The discrepancy between SM-based and GNSS-based permanent offsets as a function of the latter. Diamonds, triangles, and squares indicate east–west, north–south, and up–down components of motion, respectively. Japan and Parkfield sites are shown by empty and filled symbols, respectively.

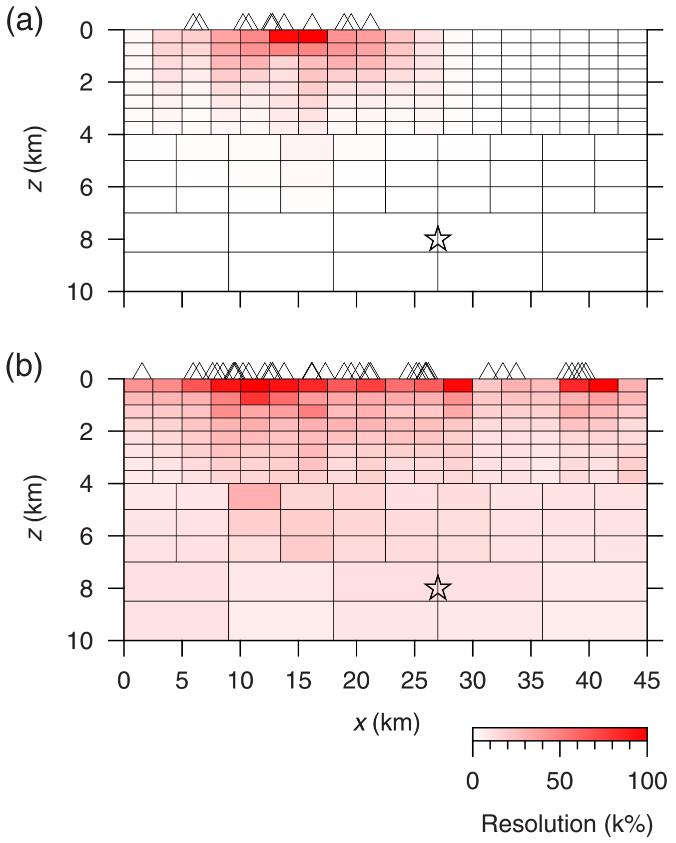

Figure 6. Model resolution. (a) The diagonal elements of the GNSS-only resolution matrix. (b) The diagonal elements of the combined GNSS and SM resolution matrix. The triangles indicate the along-strike projection of GNSS and SM receivers. The color version of this figure is available only in the electronic edition.

densely sampled the near-fault region. Thus, Parkfield's slip resolution may be greatly enhanced by incorporating permanent SM-based offsets into the slip inversion. The resolution enhancement introduced by incorporating the SM-based offsets is demonstrated in Figure 6, which presents the model resolution of the GNSS only and the combined GNSS and SM inversion. In computing the model resolution, we follow the standard procedure of decomposing the elastic kernel and discarding unstable singular values (e.g., Page *et al.*, 2009; Ziv, 2012). Because many of the SM accelerograms of the 2004 earthquake are known to have undergone baseline shifts (Shakal *et al.*, 2006), baseline correction is imperative.

To augment and improve the spatial coverage of permanent ground offsets associated with the 2004 Parkfield earthquake, near-field accelerograms were baseline corrected using the new scheme. Of the 59 near-field accelerometers that recorded this earthquake, only two were located in close proximity (less than 500 m) to a GNSS station. Despite the ground offset at these stations being much smaller than those considered in the Validation Using Collocated SM and GNSS Records of the Tohoku-Oki Earthquake section, the discrepancies between GNSS-based and SM-based permanent offsets at these locations are less than 25%, with an average of 12% (filled symbols in Fig. 5).

In selecting the data for fault-slip inversion, we followed a standard practice of discounting data recorded at sites (SM and GNSS) located less than 1 km from the fault trace (e.g., Kim and Dreger, 2008). Stations that are known to exhibit a nonlinear site response were also disregarded (Rubinstein, 2011). Following data selection, the combined GNSS–SM dataset consists of permanent ground offsets recorded by 12 GNSS and 26 SM stations.

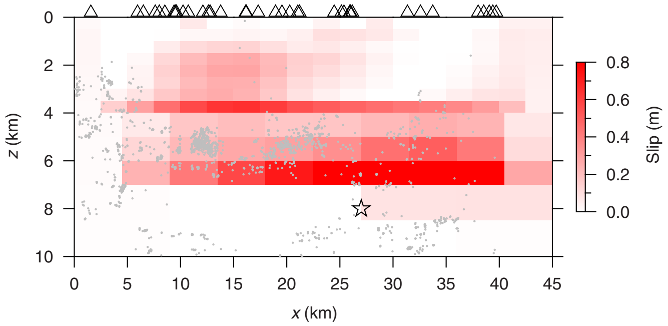

Figure 7. The preferred slip model. The star and gray dots indicate the 2004 Parkfield hypocenter and aftershocks, respectively. The triangles indicate the along-strike projection of GNSS and SM receivers. The color version of this figure is available only in the electronic edition.

We model the coseismic slip on a grid of rectangular dislocations embedded within a homogeneous elastic half-space (Okada, 1992). We implement the nonnegative least-squares optimization algorithm of Lawson and Hanson (1974) and down-weight the SM-based ground displacement inversely proportional to CF_3. We implement a smoothing constraint and identify the preferred solution with the corner of the L curve. The preferred slip distribution, shown in Figure 7, fits 85% of the combined GNSS–SM dataset. Its equivalent moment magnitude equals M_w 6.0, in agreement with previous seismological estimates for this earthquake. According to this model, most of the slip is concentrated along a narrow strip located at a depth between 5 and 7 km extending out to 20 and 12 km to the northwest and southeast of the hypocenter, respectively. The amplitude and extent of slip northwest of the hypocenter are in good agreement with previous GNSS-only static models (Johanson *et al.*, 2006; Langbein *et al.*, 2006; Barbot *et al.*, 2009; Page *et al.*, 2009). In contrast, the large seismic moment release near the hypocenter and to its south is not reported in those studies. Inspection of Figure 6 reveals that incorporating offsets derived from the Parkfield's SM dataset dramatically increases the resolution power of the inversion, in particular along deep (>6 km) segments located near the 2004 hypocenter. This suggests that inferred slip occurring near and to the southeast of the 2004 hypocenter is a robust feature of the inversion.

Because Parkfield's ground shaking peaked in two main lobes (Fig. 8a), so do the coseismic slip distributions resulting from kinematic inversions that utilize SM data (Custódio *et al.*, 2005, 2009; Kim and Dreger, 2008; Twardzik *et al.*, 2012). Typically in those models, the southernmost slip patch is located very close to the epicenter. Nevertheless, both the amplitude and the spatial extent of that slip patch differ markedly from what is inferred in this study (Fig. 7). Such discrepancies may be attributed to differences in the frequency content of the input data. Kinematic models relying on SM data can only resolve periods shorter than the total source duration and hence lack the sensitivity to the amplitude of coseismic finite slip. Our model incorporates permanent

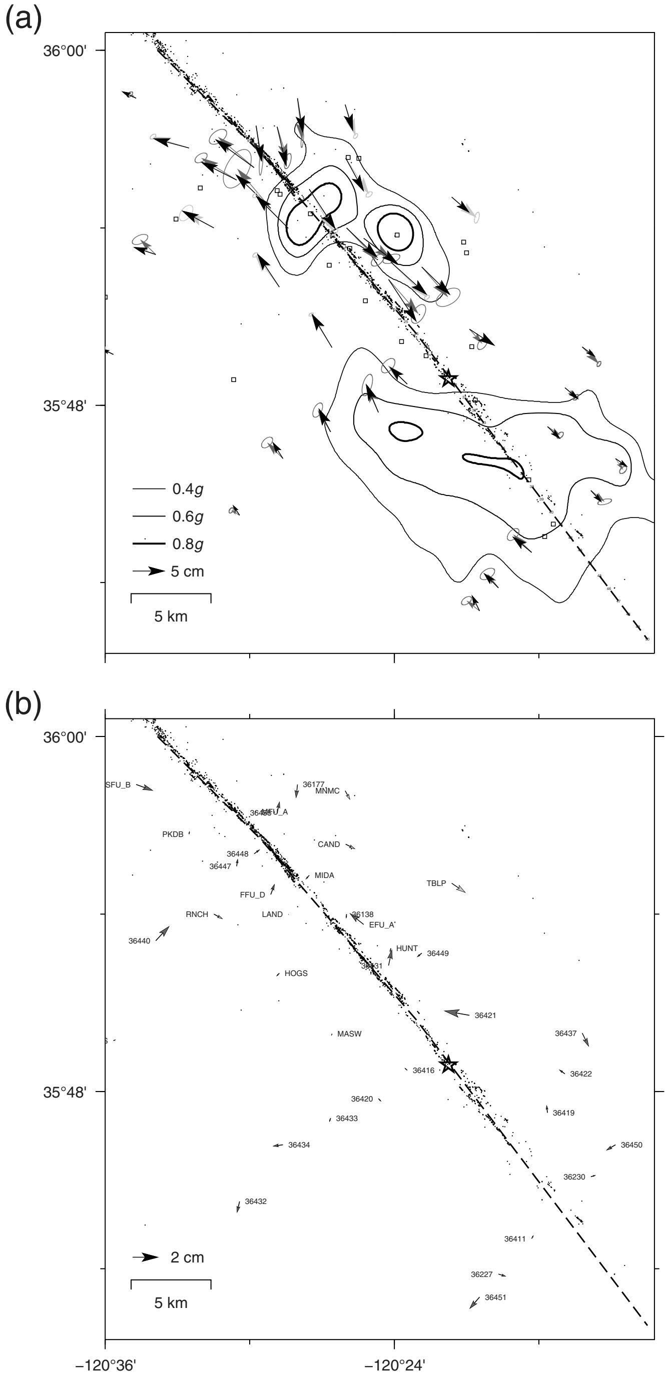

Figure 8. Permanent ground offsets from baseline-corrected accelerometers and GNSS sites recording the 2004 Parkfield mainshock. (a) Data and model output. (b) Residuals between observed and modeled displacements. Dark gray, light gray, and black arrows are for GNSS input, SM input, and modeled horizontal displacements, respectively. Star and black dots show the epicenter and background seismicity, respectively. Dashed line indicates the surface trace of the model fault. Contours indicate peak ground motion. Squares are for stations not used in the source inversion.

offsets from several sites located at short epicentral distances and is therefore able to reliably image static slip in that area. We conclude that the identification of slip near the hypocenter and to its south in our combined GNSS-SM dataset inversion is made possible thanks to the addition of the SM-based ground offsets. The spatial extent of that slip patch is in good agreement with that of the Parkfield aftershocks (Ziv, 2012).

SUMMARY

An approach for automatic extraction of permanent ground offsets from near-field SM records is introduced. Its main advantage with respect to previous schemes (e.g., Iwan *et al.*, 1985; Boore, 2001; Wu and Wu, 2007; Wang *et al.*, 2011) is that it corrects for source time functions of arbitrary shape and level of complexity, and its main novelty is the addition of a constraint on the slope of the ground-velocity spectra at long periods.

The new scheme is validated using accelerograms of the 2011 M_w 9 Tohoku-Oki and the 2004 M_w 6.0 Parkfield earthquakes. It successfully recovers the true offsets over a range of 0.01–5 m, with an average discrepancy between GNSS-based and SM-based offsets of about 10%.

Finally, to augment and improve the spatial coverage of permanent ground offsets associated with the 2004 Parkfield earthquake, near-field accelerograms were baseline corrected using the new scheme. To satisfy permanent offsets to the southeast of the epicenter, slip is required to extend to about 5 km into the Cholame section of the SAF. This may explain the strong shaking in that area.

DATA AND RESOURCES

Seismic data used in this study were recorded and maintained by the National Research Institute for Earth Science and Disaster Resilience (NIED) strong-motion (SM) seismograph networks K-net and KiK-net (doi: 10.17598/NIED.0004; last accessed April 2019). Data are from Global Navigation Satellite Systems (GNSS) sites processed by Ruhl *et al.* (2019), which are available at https://zenodo.org/record/1434374 (last accessed December 2019). The 2004 Parkfield GNSS offsets are calculated from daily solutions obtained by Scripps Orbit and Permanent Array Center (SOPAC; http://sopac-csrc.ucsd.edu, last accessed December 2012).

ACKNOWLEDGMENTS

The authors thank two anonymous reviewers and associate editor Adrien Oth for providing comments that improved the quality of this article.

REFERENCES

Aki, K., and P. Richards (2002). *Quantitative Seismology*, University Science Books, Sausalito, California.

Bakun, W. H., and A. Lindh (1985). The Parkfield, California earthquake prediction experiment, *Science* **229,** 4714.

Barbot, S., Y. Fialko, and Y. Bock (2009). Postseismic deformation due to the M_w 6.0 2004 Parkfield earthquake: Stress-driven creep on a fault with spatially variable rate-and-state friction parameters, *J. Geophys. Res.* **114,** no. B07405, 1–26, doi: 10.1029/2008JB005748.

Bock, Y., D. Melgar, and B. W. Crowell (2011). Real-time strong-motion broadband displacements from collocated GPS and accelerometers, *Bull. Seismol. Soc. Am.* **101,** no. 6, 2904–2925, doi: 10.1785/0120110007.

Boore, D. M. (2001). Effect of baseline corrections on displacements and response spectra for several recordings of the 1999 Chi-Chi, Taiwan, earthquake, *Bull. Seismol. Soc. Am.* **91,** no. 5, 1199–1211, doi: 10.1785/0120000703.

Boore, D. M., C. D. Stephens, and W. B. Joyner (2002). Comments on baseline correction of digital strong-motion data: Examples from the 1999 Hector Mine, California, earthquake, *Bull. Seismol. Soc. Am.* **92,** no. 4, 1543–1560, doi: 10.1785/0120000926.

Brune, J. N. (1970). Tectonic stress and the spectra of seismic shear waves from earthquakes, *J. Geophys. Res.* **75,** no. 26, 4997–5009, doi: 10.1029/JB075i026p04997.

Custódio, S., P. Liu, and R. J. Archuleta (2005). The 2004 M_w 6.0 Parkfield, California, earthquake: Inversion of near-source ground motion using multiple data sets, *Geophys. Res. Lett.* **32,** no. L23312, 1–4, doi: 10.1029/2005GL024417.

Custódio, S., M. T. Page, and R. J. Archuleta (2009). Constraining earthquake source inversions with GPS data: 2. A two-step approach to combine seismic and geodetic data sets, *J. Geophys. Res.* **114,** no. B01315, 1–20, doi: 10.1029/2008JB005746.

Emore, G. L., J. S. Haase, K. Choi, K. M. Larson, and A. Yamagiwa (2007). Recovering seismic displacements through combined use of 1-Hz GPS and strong-motion accelerometers, *Bull. Seismol. Soc. Am.* **97,** no. 2, 357–378, doi: 10.1785/0120060153.

Graizer, V. M. (1979). Determination of the true ground displacement by using strong motion records, *Izvestiya Phys. Solid Earth* **15,** 875–885.

Iwan, W. D., M. A. Moser, and C.-Y. Peng (1985). Some observations on strong-motion earthquake measurement using a digital accelerograph, *Bull. Seismol. Soc. Am.* **75,** no. 5, 1225–1246.

Johanson, I. A., E. J. Fielding, F. Rolandone, and R. Bürgmann (2006). Coseismic and postseismic slip of the 2004 Parkfield earthquake from space-geodetic data, *Bull. Seismol. Soc. Am.* **96,** no. 4B, S269–S282, doi: 10.1785/0120050818.

Kim, A., and D. S. Dreger (2008). Rupture process of the 2004 Parkfield earthquake from near-fault seismic waveform and geodetic records, *J. Geophys. Res.* **113,** no. B07308, 1–16, doi: 10.1029/2007JB005115.

Langbein, J., J. R. Murray, and H. A. Snyder (2006). Coseismic and initial postseismic deformation from the 2004 Parkfield, California, earthquake, observed by global positioning system, electronic distance meter, creepmeters, and borehole strainmeters, *Bull. Seismol. Soc. Am.* **96,** no. 4B, 304–320, doi: 10.1785/0120050823.

Lawson, C., and B. Hanson (1974). *Solving Least Squares Problems*, Prentice-Hall, Philadelphia, Pennsylvania.

Madariaga, R. (1976). Dynamics of an expanding circular fault, *Bull. Seismol. Soc. Am.* **66,** no. 3, 639–666.

Madariaga, R., S. Ruiz, E. Rivera, F. Leyton, and J. C. Baez (2018). Near-field spectra of large earthquakes, *Pure Appl. Geophys.* **176,** 1–19, doi: 10.1007/s00024-018-1983-x.

Melgar, D., Y. Bock, D. Sanchez, and B. W. Crowell (2013). On robust and reliable automated baseline corrections for strong motion seismology, *J. Geophys. Res.* **118,** no. 3, 1177–1187, doi: 10.1002/jgrb.50135.

Nikolaidis, R. M., Y. Bock, P. J. de Jonge, P. Shearer, D. C. Agnew, and M. Van Domselaar (2001). Seismic wave observations with the Global Positioning System, *J. Geophys. Res.* **106,** no. B10, 21,897–21,916, doi: 10.1029/2001JB000329.

Okada, Y. (1992). Internal deformation due to shear and tensile faults in a half-space, *Bull. Seismol. Soc. Am.* **82,** no. 2, 1018–1040.

Page, M. T., S. Custódio, R. J. Archuleta, and J. M. Carlson (2009). Constraining earthquake source inversions with GPS data: 1. Resolution-based removal of artifacts, *J. Geophys. Res.* **114,** no. B01314, 1–13, doi: 10.1029/2007JB005449.

Rubinstein, J. L. (2011). Nonlinear site response in medium magnitude earthquakes near Parkfield, California, *Bull. Seismol. Soc. Am.* **101,** no. 1, 275–286, doi: 10.1785/0120090396.

Ruhl, C. J., D. Melgar, J. Geng, D. E. Goldberg, B. W. Crowell, R. M. Allen, Y. Bock, S. Barrientos, S. Riquelme, J. C. Baez, *et al.* (2019). A global database of strong-motion displacement GNSS recordings and an example application to PGD scaling, *Seismol. Res. Lett.* **90,** no. 1, 271–279, doi: 10.1785/0220180177.

Segall, P. (2010). *Earthquake and Volcano Deformation*, Princeton University Press, Princeton, New Jersey.

Shakal, A., H. Haddadi, V. Graizer, K. Lin, and M. Huang (2006). Some key features of the strong-motion data from the **M** 6.0 Parkfield, California, earthquake of 28 September 2004, *Bull. Seismol. Soc. Am.* **96,** no. 4B, S90–S118, doi: 10.1785/0120050817.

Sieh, K. E. (1978). Central California foreshocks of the Great 1857, *Bull. Seismol. Soc. Am.* **68,** no. 6, 1731–1749.

Twardzik, C., R. Madariaga, S. Das, and S. Custódio (2012). Robust features of the source process for the 2004 Parkfield, California, earthquake from strong-motion seismograms, *Geophys. J. Int.* **191,** no. 3, 1245–1254, doi: 10.1111/j.1365-246X.2012.05653.x.

Vidale, J. E., S. Goes, and P. G. Richards (1995). Near-field deformation seen on distant broadband seismograms, *Geophys. Res. Lett.* **22,** no. 1, 1–4, doi: 10.1029/94GL02893.

Wang, R., S. Parolai, M. Ge, M. Jin, T. R. Walter, and J. Zschau (2013). The 2011 M_w 9.0 Tohoku earthquake: Comparison of GPS and strong-motion data, *Bull. Seismol. Soc. Am.* **103,** no. 2B, 1336–1347, doi: 10.1785/0120110264.

Wang, R., B. Schurr, C. Milkereit, Z. Shao, and M. Jin (2011). An improved automatic scheme for empirical baseline correction of digital strong-motion records, *Bull. Seismol. Soc. Am.* **101,** no. 5, 2029–2044, doi: 10.1785/0120110039.

Wu, Y.-M., and C.-F. Wu (2007). Approximate recovery of coseismic deformation from Taiwan strong-motion records, *J. Seismol.* **11,** no. 2, 159–170, doi: 10.1007/s10950-006-9043-x.

Ziv, A. (2012). Inference of coseismic slip via joint inversion of GPS and aftershock data: The 2004 Parkfield example, *J. Geophys. Res.* **117,** no. 3, 1–7, doi: 10.1029/2011JB008400.

Manuscript received 21 January 2020